Catalysis Today 158 (2010) 139–145

Contents lists available at ScienceDirect

Catalysis Today

journal homepage: www.elsevier.com/locate/cattod

Surface active sites in alumina-supported MoVNbTeO oxide catalysts

R. López-Medina[a,b], H. Golinska[b], M. Ziolek[b], M.O. Guerrero-Pérez[c], M.A. Bañares[a,*]

[a] Catalytic Spectroscopy Laboratory, Instituto de Catálisis y Petroleoquímica, CSIC, Marie Curie 2, E-29049 Madrid, Spain
[b] Adam Mickiewicz University, Faculty of Chemistry, Grunwaldzka 6, 60-780 Poznań, Poland
[c] Departamento de Ingeniería Química. Escuela de Ingenierías., Universidad de Málaga, E-29071 Málaga, Spain

ARTICLE INFO

Article history:
Available online 2 August 2010

Keywords:
Methanol oxidation
Propane oxidation
Acrylic acid
Active sites
Mo–V–O catalysts
Surface properties
Nanocrystalline

ABSTRACT

Methanol oxidation reaction probes the chemical nature of the active sites (formaldehyde forms on surface redox sites and dimethylether, on acidic ones) and has been used to characterize the active sites present on the surface of Mo–V–Nb–O catalysts which has been correlated with the activity for propane oxidation to acrylic acid. The effect of calcination atmosphere and the role of tellurium addition have been discussed as a function of the total coverage. The structure of Mo–V–O mixed phases strongly depends on these parameters, as determined by XRD, XPS and Raman spectroscopy. Such structures determine the catalytic behavior of catalysts during both propane and methanol oxidation. At low and medium coverages, the presence of oxidized dispersed surface vanadium structures (VOx) determines the catalytic behavior; such phases are active for methanol oxidation to formaldehyde. At high coverages, the formation of Al–Mo–O and Mo–V–O crystalline aggregates decreases the number of redox sites, whereas the presence of reduced species in rutile-like and/or MoO_2 increases the redox activity for inert-calcined samples. For samples with high coverage, tellurium addition decreases the activity during methanol oxidation. This is due to a decrease in the population of surface VOx species. The interaction of tellurium with molybdenum and vanadium sites results in mixed phases with intermediate oxidation state that exhibit higher yields to acrylic acid.

© 2010 Elsevier B.V. All rights reserved.

1. Introduction and objectives

Understanding the factors that determine surface reactivity is necessary to design new and more effective catalytic processes [1]. Methanol is a well-established probe to determine the number of surface active sites present in metal oxide catalysts and the distribution of acid–basic and redox sites [1–5]. Methanol oxidation over metal oxides produces different reaction products depending on the surface active site: formaldehyde on surface redox sites, dimethylether on surface acidic sites, and CO_2 on surface basic sites [6–9]. Combination of acid and redox or basic and redox sites will produce dimethoxymethane or methyl formate, respectively [10,11].

Mo–V–O oxides are active and selective in several oxidation reactions, like the direct conversion of propane into acrylonitrile or acrylic acid, or the propane ammoxidation to acrylonitrile [12,17]. Upon addition of Te and/or Nb, these oxides can present two main phases, named M1 and M2 [13–17]. The M1 phase is associated with the selective activation of propane into acrylic acid (oxidation) and acrylonitrile (ammoxidation) [18,15,19]. Niobium oxide is an interesting additive since it easily reacts with many other metal oxides resulting in phases that are important for the activation of alkanes [15,17,20–22].

This paper studies several supported Te- and Nb-doped Mo–V–O catalysts, and the role of total coverage and calcination under different atmospheres on their structural and reactive features. The catalysts are characterized by XRD, XPS and Raman spectroscopy whereas the nature of the active sites is analyzed by methanol oxidation. These catalysts have been tested for propane partial oxidation to acrylic acid.

2. Experimental

The synthesis of alumina-supported MoVNbTeO mixed metal oxide catalysts were prepared from an aqueous slurry comprising molybdenum $(NH_4)_6Mo_7O_{24}{\cdot}4H_2O$ (Sigma–Aldrich), vanadium NH_4VO_3 (Sigma–Aldrich), niobium (ammonium niobium soluble complex; Niobium Products) and tellurium (telluric acid $TeOH_6$ Sigma–Aldrich) in the appropriate atomic ratios with an surface atoms density of 4, 8 and 12 MoVNbTe atoms/nm^2 (A) denominated as "A"$Mo_xV_yNb_wTe_z$ using tartaric acid as complexing agent. The support (15 g γ-Al_2O_3 Sasol Puralox SCCa-5/200) was added to a solution containing the slurry and then was evaporated to dry-

* Corresponding author at: Catalytic Spectroscopy Laboratory, Instituto de Catálisis y Petroleoquímica, CSIC; Marie Curie 2, Campus Cantoblanco, E-29049-Madrid, Spain. Tel.: +34 91 585 4788; fax: +34 91 585 4760.
E-mail address: banares@icp.csic.es (M.A. Bañares).

0920-5861/$ – see front matter © 2010 Elsevier B.V. All rights reserved.
doi:10.1016/j.cattod.2010.06.015

ness at 80 °C. The product was dried at 110 °C overnight in ambient air. The thermal treatments in air or nitrogen were performed at a heating rate of 5 °C/min up to 600 °C for 2 h. The catalysts are denoted as "–air" and "–inert", depending of this final heat treatment in air or N_2, respectively. For reference purposes, the same procedure was used, without addition of alumina support, for the preparation of a MoVNbTe rutile sample. All catalysts were sieved to 0.5–1 mm.

The partial oxidation of methanol reaction was performed in a tubular fixed-bed reactor with a coaxial thermocouple pocket under atmospheric pressure. The reactor was placed in an electrical oven for the experiments. The samples were activated in helium flow (40 ml/min) at 400 °C for 2 h. The catalyst weight was 100 mg and the reaction feed consisted of 40 ml/min of He/O_2/MeOH (88/8/4 mol%) (mass flow controller). The experiments were carried out in the 250–300 °C reaction temperatures range. Heated lines take reaction products to an on-line gas chromatograph GC 8000 Top equipped with a capillary column of DB-1 fitted to a FID detector, and Porapak Q and 5A molecular sieves columns, to a TCD detector.

The partial oxidation of propane was carried out at atmospheric pressure in a flow-type fixed-bed microreactor. Typical reaction conditions were: GHSV = 4800 h^{-1}; catalyst amount 200 mg; temperature range 350–450 °C; feed gas (vol.%), propane/O_2/H_2O/He = 12.5/20.4/15.9/51.2. Reaction products were analyzed on line with a Varian 3800 gas chromatograph equipped with a flame ionization and thermal conductivity detectors.

The BET surface areas of catalysts were measured using a Micromeritics ASAP 2000 analyzer by nitrogen adsorption at liquid nitrogen temperature. The samples were previously outgassed under nitrogen flow at 140 °C. The XRD patterns were recorded in the 2θ = 4–90° range before and after calcination treatments in a Seifert 3000P XRD diffractometer using CuKα radiation (λ = 0.15418 nm) and a graphite monochromator (40 kV, 30 mA, and scanning rate of 2°/min for Bragg's angles). Raman spectroscopy was performed with a Renishaw System 1000 spectrometer equipped with green laser (Spectra Physics, λ = 514 nm, power 19 mW, 1 mW on sample). For Raman spectra, the fresh catalysts were dehydrated *in situ* in dry air stream (50 ml/min) at 200 °C. The spectra were obtained under dehydrated conditions (ca. 200 °C) in a hot stage (Linkam TS-1500). The Raman spectra of the catalysts were also obtained under ambient hydrated conditions. *In situ* Raman spectroscopy was performed at various temperatures from 50 to 600 °C with a ramp of 10 °C/min) on the supported MoVNb oxide catalysts.

X-ray photoelectron spectroscopy (XPS) spectra were recorded on a VG Escalab 200R spectrometer equipped with a hemispherical electron analyzer and a MgKα ($h\nu$ = 1254.6 eV, 1 eV = 1.6302×10^{-19} J) X-ray source powered at 120 W. The sample powders were pressed into small copper supports and then mounted on a support rod placed in the pre-treatment chamber. Prior to the analysis, oxide samples were evacuated at 25 °C for 2 h under atmospheric pressure. The X-ray chamber was evacuated to 1×10^{-6} Pa. As a reference, we used the C 1 s signal of the adventitious carbon (carbon of any surface adsorbed), which we fixed at 284.6 eV. The latter procedure involved linear background subtraction and a curve-fitting using a mixed Gaussian–Lorentzian function. The quantitative analysis was based on the areas of the XPS peaks, which was corrected on the atomic sensitivity factor of the corresponding elements and the area of peaks was determined after subtraction of background by Shirley method with an error χ^2 minimum. The spectra of Mo 3d level were decomposed into peak couples with parameters of spin–orbit separation ΔE_p (Mo $3d_{5/2}$–Mo $3d_{3/2}$) = 3.15 eV, ΔE_p (Te $3d_{5/2}$–Te $3d_{3/2}$) = 10.4 eV. The deconvolution of Te $3d_{5/2}$ peaks showed that all of the peaks can be fitted into two components. Measurement error of the spectra was ±0.1 eV. Due to X-ray irradiation and vacuum conditions, transition metal oxides tend to reduce partially. Thus, the average oxidation state is moderately lower than in reality. However, it is possible to compare relative population of different oxidation states.

UV–vis DRS spectra are obtained by taking using a halon white (PTFE) reflectance standard in an AvaLight DHS spectrometer equipment with a Deuterium-Halogen light source, 215–2500 nm, TTL shutter and SR fiber optic. Reflectance data were converted to the absorption spectra using Kubelka–Munk function F(R). The thickness of the catalyst bed was 2 mm, and the amount of the catalyst used was around 20 mg. The γ-Al_2O_3 support possesses no absorbance in the region of interest.

3. Results

Table 1 lists the BET areas of the samples; which decrease with total coverage, as expected. These are similar at low and medium coverages, regardless of calcination treatments. At high coverages (12 atoms/nm^2), the BET surface area values obtained for the inert-calcined series are significantly higher that those of the air-calcined series.

The XPS binding energies are listed in Table 1. The binding energies for niobium are characteristic of Nb^{5+} species [23,24] and show little changes in the different series. The binding energies values of the Te $3d_{5/2}$ peak are typical of Te^{6+} species [25,26] with a minor contribution of lower oxidation state (Te^{4+}). A small amount of reduced Te^{4+} species is detected in all the Te-containing samples, their concentration is higher in the case of inert-calcined samples. For the molybdenum X-ray photoelectron spectra deconvolution, the spin–orbit splitting between the Mo $3d_{5/2}$ and Mo $3d_{3/2}$ signals was fixed to 3.1 eV and the intensity ratio was set to 0.67. Three different molybdenum species can be identified in the XPS spectra, characteristic of Mo^{6+}, Mo^{5+} and Mo^{4+} species [27–30]. Reduced Mo^{4+} species are only detected for inert calcination. The $3d_{3/2}$ and $3d_{5/2}$ shoulder peaks are at 234.7 and 231.3–231.7 eV, which can be assigned to the Mo^{5+} state, whose concentration increases for inert-calcined series. V 2p BE region typically exhibits two components; the one at higher binding energies (516.9–517.0 eV) is assigned to V^{5+} sites [31]; a second component, at lower binding energy (516.1–516.3) is associated with V^{4+} species [32]; and a third component at lower BE values (515.4 eV) corresponds to reduced V^{3+} species [24,25]. V^{4+} population, in general, is higher for inert-calcined samples. A rather unique sample is $12Mo_5V_4Nb_1$–inert, which possesses a significant population of V^{4+} species and no V^{5+} sites. The presence of tellurium has a clear effect on vanadium sites upon inert calcination, in which a significant fraction remains as V^{5+}, unlike the Te-free inert-calcined series.

Fig. 1 shows the XRD patterns, which shape depends on the calcination atmosphere. In the case of air-calcined samples (A and B), several peaks in the 22–30° range, corresponding to Al–Mo–O, Mo–Nb–O and Mo–V–O mixed phases, are evident at high coverages. The Mo_5O_{14}-type structure [33,34] can be identified by its strongest reflections at 22.1° and 24.9° that in this case can overlap with the other signals, thus, the presence of such oxide cannot be excluded. MoO_2 and a rutile Mo–V–Nb–O phase are detected at high loadings in inert-calcined samples. The rutile phase exhibit high intensity peaks at 26.6, 36.8, 38.0, 41.6 and broad peaks at 53.9, 62.0, 67.9, 72.0 and 80.3° [35–37]. The main diffraction peaks of MoO_2 [38] and the rutile Mo–V–O diffraction patterns overlap at 26.6°, 36.8° and 53.9°. In addition, the peak at 68°, assigned to the rutile Mo–V–O structure, overlaps with the diffraction peaks corresponding to the alumina support. Thus, rutile

Table 1
BET areas and XPS (in eV) results for MoVTeNb (the values in parentheses indicates the percentage of peaks obtained during deconvolution).

Catalyst	$Nb^{5+}{}_{3d5/2}$	$Te^{6+}{}_{3d5/2}$	$Te^{4+}{}_{3d5/2}$	$Mo^{6+}{}_{3d5/2}$	$Mo^{5+}{}_{3d5/2}$	$Mo^{4+}{}_{3d5/2}$	$V^{5+}{}_{2p3/2}$	$V^{4+}{}_{2p3/2}$	$V^{3+}{}_{2p3/2}$	S_{BET} (m^2/g)
$4Mo_5V_4Nb_1$–air	207.1	–	–	232.8 (85.1)	231.7 (14.9)	–	517.4 (89.2)	516.1 (10.8)	–	165
$8Mo_5V_4Nb_1$–air	207.1	–	–	232.9 (89.7)	231.7 (10.3)	–	517.6 (94.1)	516.3 (5.9)	–	110
$12Mo_5V_4Nb_1$–air	207.3	–	–	232.9 (90)	231.8 (10)	–	517.5 (100)	–	–	54
$4Mo_5V_4Nb_1$–inert	207.3	–	–	233.1 (66.2)	232.0 (33.8)	–	517.1 (100)	–	–	172
$8Mo_5V_4Nb_1$–inert	206.8	–	–	233.2 (40.3)	231.3 (34.5)	229.3 (25.2)	516.8 (59.8)	515.4 (40.2)	–	157
$12Mo_5V_4Nb_1$–inert	207.3	–	–	233.2 (40.8)	231.0 (20.2)	229.1 (39.0)	–	516.1 (100)	–	128
$4Mo_5V_4Nb_{0.5}Te_{0.5}$–air	206.8	577.0 (90.3)	574.2 (9.7)	232.8 (88.3)	231.7 (11.7)	–	517.3 (90.0)	516.3 (10.0)	–	159
$8Mo_5V_4Nb_{0.5}Te_{0.5}$–air	207.0	576.4 (92.1)	574.2 (7.9)	232.8 (93.0)	231.7 (7.0)	–	517.5 (92.0)	516.3 (4.1)	515.3 (3.9)	129
$12Mo_5V_4Nb_{0.5}Te_{0.5}$–air	207.1	577.0 (93.7)	574.2 (6.3)	232.6 (94.0)	231.7 (6.0)	–	517.5 (100)	–	–	74
$4Mo_5V_4Nb_{0.5}Te_{0.5}$–inert	206.9	576.8 (87.7)	574.2 (12.3)	233.0 (60.2)	231.7 (30.2)	229.5 (9.6)	517.0 (88.3)	516.3 (11.7)	–	169
$8Mo_5V_4Nb_{0.5}Te_{0.5}$–inert	206.8	576.8 (89.6)	574.2 (10.4)	233.1 (43.7)	231.7 (30.2)	229.4 (26.1)	517.0 (63.0)	516.7 (37.0)	–	150
$12Mo_5V_4Nb_{0.5}Te_{0.5}$–inert	207.0	576.9 (86.4)	574.3 (13.6)	233.0 (50.9)	231.6 (39.1)	229.5 (10.0)	517.1 (70.4)	516.7 (29.6)	–	123

Mo–V oxide phase can only be identified by the diffraction peak near 26.4°, which is visible in samples with the highest coverage.

Upon tellurium doping, air-calcined samples (Fig. 1B) show similar diffraction patterns the same phases than undoped ones (Fig. 1A, dominated by $Al_2(MoO_4)_3$), and new peaks at 22.1°, 28.3°, 36.2°, 50.0° and 55.0° show the presence of hexagonal $Te_{0.33}MO_{3.33}$ with M = Mo, V and/or Nb. In the case inert-calcined samples (Fig. 1D), the diffractograms are also dominated by the peaks of the rutile and MoO_2 diffractions, as in the case of samples without Te; but the peaks of the rutile phase are more intense, and are develop at lower coverages (Fig. 1D). A peak near 22.1° is also detected in the samples with high coverage that was not detected in the samples without Te, it may belong to the M1 phase (orthorhombic $Te_2M_{20}O_{57}$ structure) [39–41], which presents peaks at 6.6°, 7.9°, 9.0°, 22.1°, 27.3° and 45.3°.

Fig. 2 shows representative Raman spectra of the catalysts. Air-calcined samples exhibit a strong signal near 990–1030 cm^{-1}, characteristic of the stretching modes of Mo=O and/or V=O bonds, respectively. The broad band exhibits a maximum neat1000 cm^{-1} that is characteristic of the Mo=O mode. It is difficult to assess the relative population of these two Mo=O and V=O sites since the Raman section of molybdenum oxide species is more intense than that of vanadium oxide species. A shoulder near 1020 cm^{-1} is indicative of the V=O mode of surface vanadium species. This suggests the presence of surface molybdenum and vanadium species [42]. The Raman bands corresponding to α-MoO_3 crystalline phase (992, 817, 375, 334, 283, 234, 193 and 148 cm^{-1}) are visible in the high coverage air-calcined samples (Fig. 2A and B). The Raman bands due to MoO_2 appear at 227, 362, 494, 572 and 742 cm^{-1} [43] and are visible in Fig. 2C ($12Mo_5V_4Nb_1$–inert). The broad Raman band near 820–840 cm^{-1} corresponds to a rutile-type structure. The Raman band near 885 cm^{-1} is characteristic of Mo_5O_{14}-type structure [44,45]. In the case of Te-containing catalysts, the band at 885–890 cm^{-1} can be also assigned to the stretching mode of bridging Mo–O–M (M = Mo, V) bonds of highly distorted $Te_2M_{20}O_{57}$ on alumina [46–48]. $12Mo_5V_4Te_{0.5}$–inert exhibits Raman bands near 820 and 470 cm^{-1} (Fig. 2D(c)) which are characteristic of M1 phase [49].

The UV–vis DR spectra depend on the calcination atmosphere (Fig. 3). A strong signal is detected between 250 and 400 nm for air-calcined samples. Such band is assigned to ligand–metal charge transfer (LMCT) transitions involving primarily the charge transfer from oxygen ligands to Mo^{6+} or V^{5+} metal cations, in addition to Nb^{5+} and Te^{4+}[50,51]. This band extends up to 600 nm in the case of Te-containing samples, this additional absorption is assigned to partially reduced Mo cations [52–54]. In the case of inert-calcined samples, a band between 300 and 400 nm suggests the presence of V^{5+} species in a different environment. The broad absorption between 500 and 800 nm is typically associated with V^{4+} cations [55].

Fig. 4 shows the yields of main products during methanol oxidation and, for comparative purposes, the yield to acrylic acid obtained during propane partial oxidation has also been included. Dimethylether is the main product at low coverages during methanol oxidation, whereas formaldehyde forms at higher coverages; evidencing a transition from essentially acidic to redox properties. The methanol conversion on the air-calcined samples decreases with coverage, probably due to the presence of Al–Mo–O and Mo–V–O oxidized phases, detected by XRD (Fig. 3). For tellurium containing samples, methanol conversion decreases at high coverages, indicating that dispersed oxide species are more active for methanol activation than Te-containing samples; which is not the case for propane oxidation, which activity increases upon Te addition. Such trend is less intense at lower coverages (Table 2).

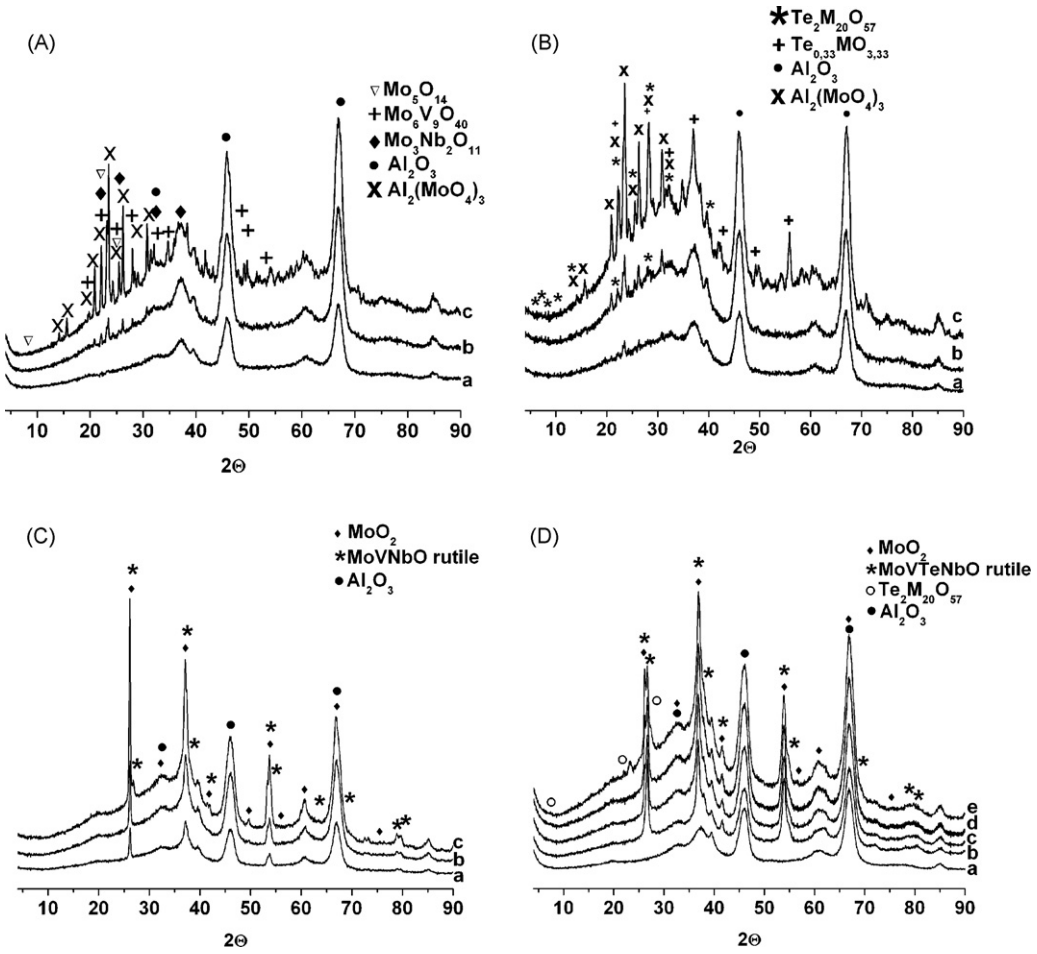

Fig. 1. X-ray diffraction pattern of (A) (a) $4Mo_5V_4Nb_1$–air, (b) $8Mo_5V_4Nb_1$–air and (c) $12Mo_5V_4Nb_1$–air; (B) (a) $4Mo_5V_4$ $Nb_{0.5}Te_{0.5}$–air, (b) $8Mo_5V_4$ $Nb_{0.5}Te_{0.5}$–air and (c) $12Mo_5V_4$ $Nb_{0.5}Te_{0.5}$–air; (C) (a) $4Mo_5V_4Nb_1$–inert, (b) $8Mo_5V_4Nb_1$–inert and (c) $12Mo_5V_4Nb_1$–inert and (D) (a) γ-Al_2O_3, (b) MoVTeNbO–rutile, (c) $4Mo_5V_4Nb_{0.5}Te_{0.5}$–inert, (d) $8Mo_5V_4$ $Nb_{0.5}Te_{0.5}$–inert and (e) $12Mo_5V_4$ $Nb_{0.5}Te_{0.5}$–inert catalysts calcinated for 2 h at 600 °C.

4. Discussion

The methanol oxidation results (Fig. 4) indicate that the catalytic behavior strongly depends on the total Mo + V + Nb + Te coverage. At low coverage (4 atoms/nm^2) the main product is dimethyl ether, indicative that the surface of catalysts is dominated by acid sites, which must belong to the hydroxyl groups from the alumina support, which are not totally titrated and to the presence of surface niobium species. Air-calcined samples present a higher yield to formaldehyde than the inert-calcined catalysts, indicative that some redox sites are present on the surface. These samples present dispersed MOx phases on their surface, which are responsible for such redox activity. Metal oxide phases are identified by Raman spectroscopy by the strong signal near 1000 cm^{-1} (Fig. 2A and B). In such phases vanadium and molybdenum are present in their highest oxidation states (Table 1). This redox activity due to surface MOx species, is able to yield formaldehyde, however, these dispersed metal oxide species are not efficient to transform the

Table 2
Catalytic activity in partial oxidation of methanol at $T = 250$ °C. These results are after 2 h of reaction.

Catalysts	Conversion % MeOH	Selectivity %				
		Formaldehyde HCHO	Methyl formate $HCOOCH_3$	Dimethyl ether CH_3OCH_3	Dimethoxy methane $(CH_3O)_2CH_2$	CO_2
$4Mo_5V_4Nb_1$–air	77.8	44.9	7.9	45.0	0.1	2.1
$8Mo_5V_4Nb_1$–air	79.4	44.4	6.7	46.3	0.3	2.3
$12Mo_5V_4Nb_1$–air	37.9	69.7	2.3	26.1	0.1	1.8
$4Mo_5V_4Nb_1$–inert	59.9	26.3	16.5	56.2	0.1	0.9
$8Mo_5V_4Nb_1$–inert	28.5	56.0	18.4	25.0	0.2	0.4
$12Mo_5V_4Nb_1$–inert	78.5	77.9	6.0	15.7	0.1	0.3
$4Mo_5V_4Nb_{0.5}Te_{0.5}$–air	58.1	46.6	15.5	37.2	0.1	0.6
$8Mo_5V_4Nb_{0.5}Te_{0.5}$–air	60.4	86.0	5.3	8.0	0.2	0.5
$12Mo_5V_4Nb_{0.5}Te_{0.5}$–air	42.1	73.1	7.8	18.0	0.6	0.5
$4Mo_5V_4Nb_{0.5}Te_{0.5}$–inert	59.2	24.5	10.4	64.0	0.1	1.0
$8Mo_5V_4Nb_{0.5}Te_{0.5}$–inert	78.2	52.9	16.4	29.8	0.3	0.6
$12Mo_5V_4Nb_{0.5}Te_{0.5}$–inert	39.1	66.7	9.1	23.8	0.2	0.2

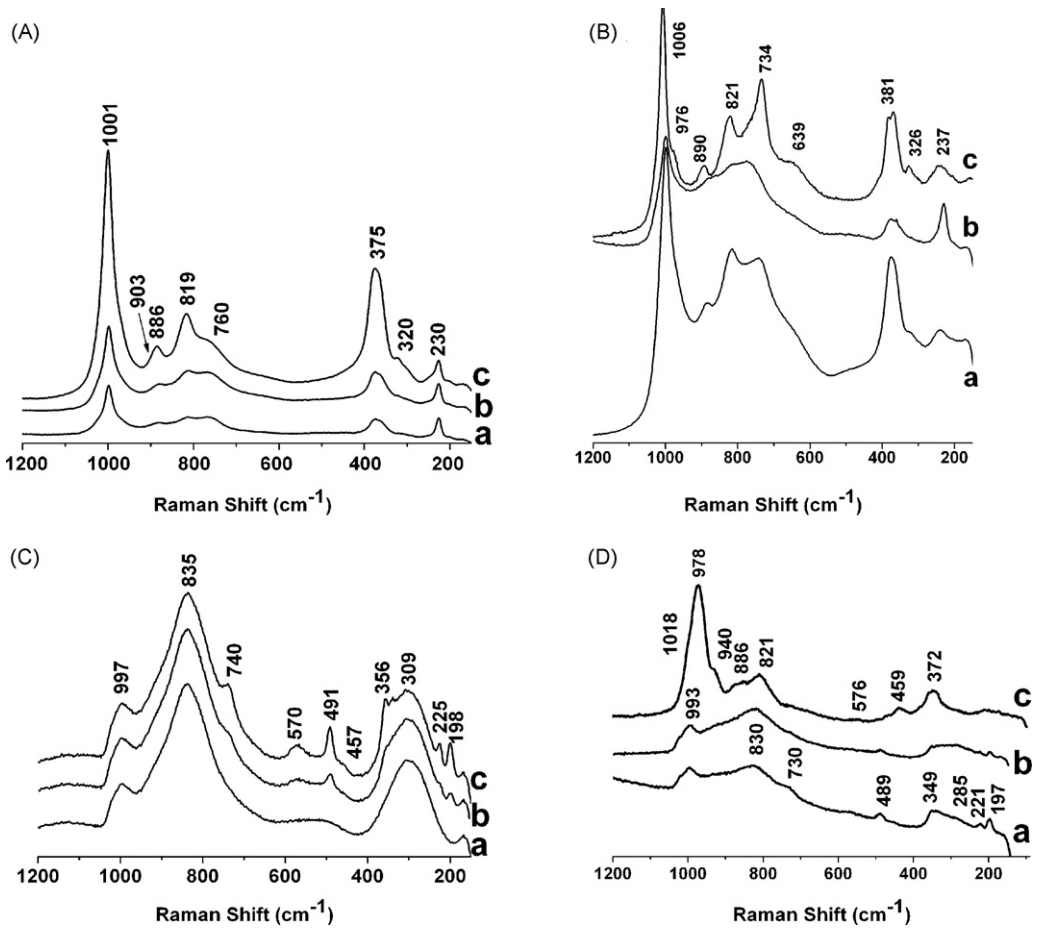

Fig. 2. Dehydrated Raman spectra of (A) (a) $4Mo_5V_4Nb_1$–air, (b) $8Mo_5V_4Nb_1$–air and (c) $12Mo_5V_4Nb_1$–air; (B) (a) $4Mo_5V_4Nb_{0.5}Te_{0.5}$–air, (b) $8Mo_5V_4Nb_{0.5}Te_{0.5}$–air, (c) $12Mo_5V_4Nb_{0.5}Te_{0.5}$–air; (C) (a) $4Mo_5V_4Nb_1$–inert, (b) $8Mo_5V_4Nb_1$–inert, (c) $12Mo_5V_4Nb_1$–inert and (D) (a) $4Mo_5V_4Nb_{0.5}Te_{0.5}$–inert, (b) $8Mo_5V_4Nb_{0.5}Te_{0.5}$–inert and (c) $12Mo_5V_4Nb_{0.5}Te_{0.5}$–inert at 200 °C.

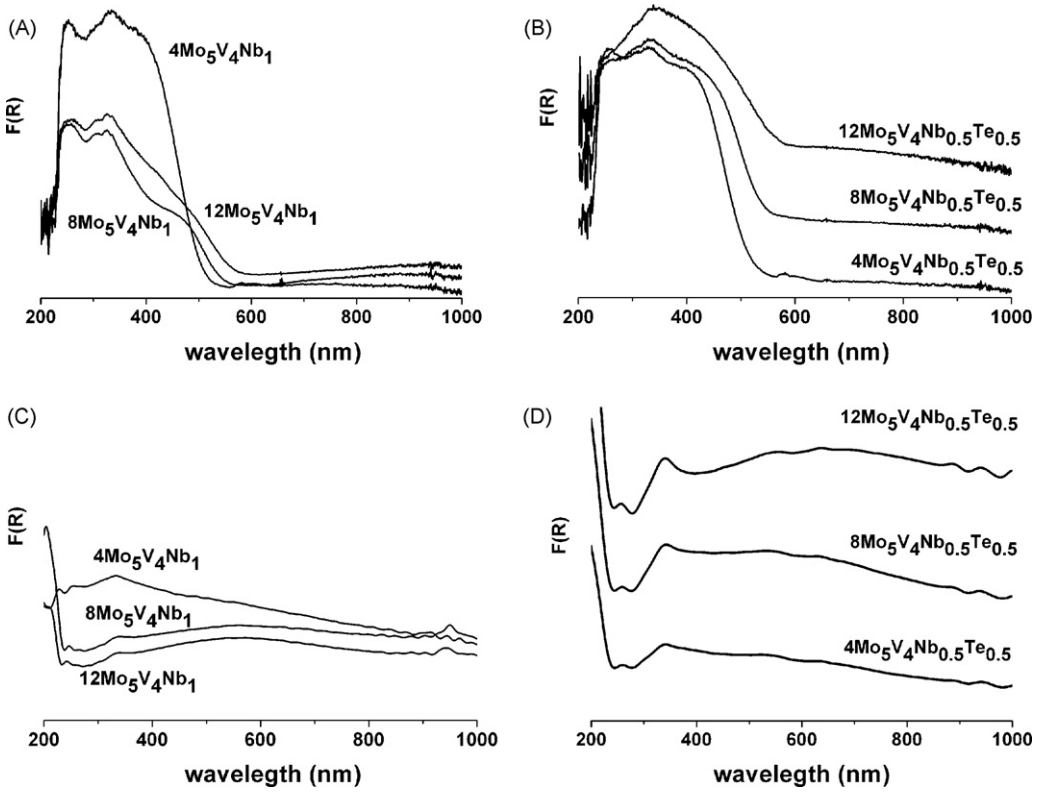

Fig. 3. Diffuse reflectance UV–vis DRS spectra for supported MoVNb(Te)O catalysts calcined in air (A and B) and nitrogen (C and D) for 2 h at 600 °C.

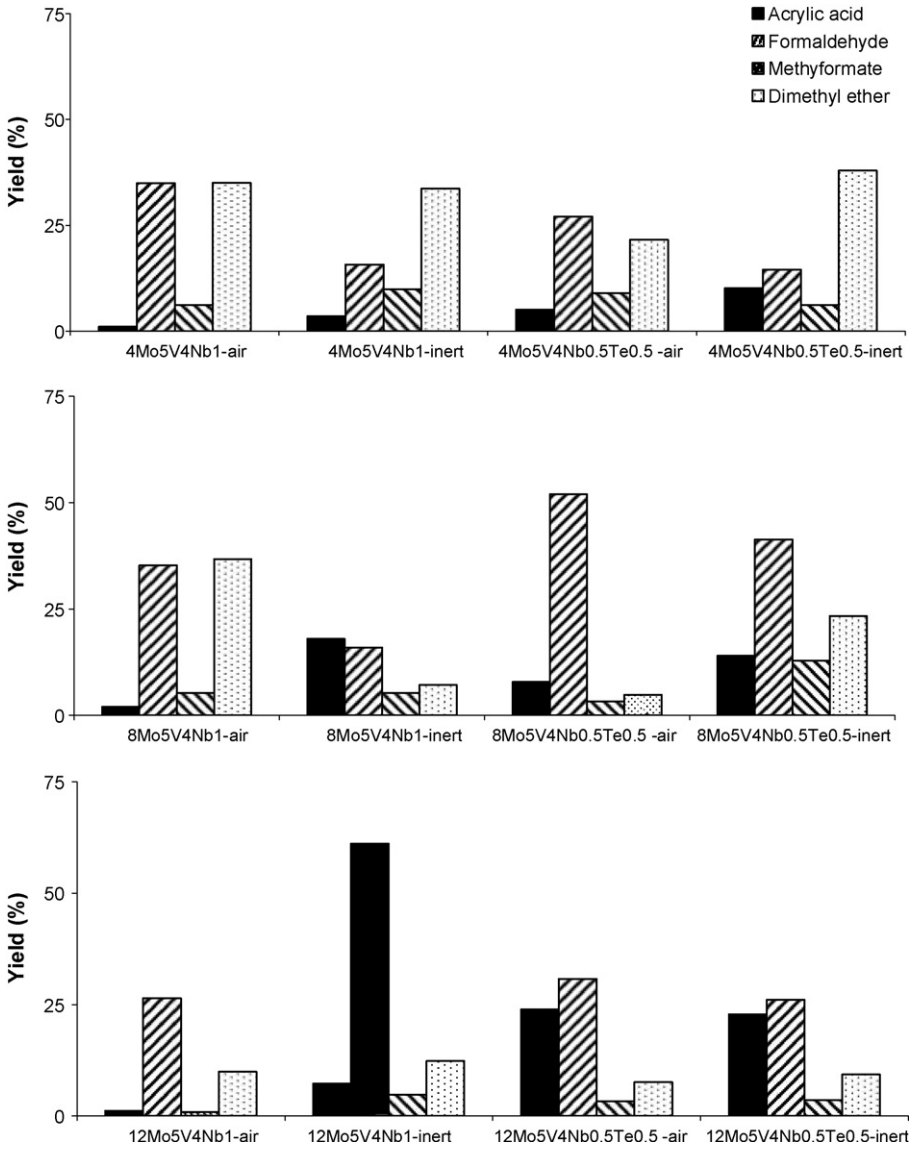

Fig. 4. Catalytic results (yields of formaldehyde, dimethylformate and dimethylether) obtained in selective oxidation of methanol, reaction conditions: total flow 40 ml/min, molar ratio $He/O_2/MeOH = 88/8/4$ mol%, 100 mg of catalyst, $T = 250\,^{\circ}C$; and yield to acrylic acid obtained during the propane partial oxidation, reaction conditions: total flow 40 ml/min feed gas (vol.%) $C_3/O_2/H_2O/He = 12.5/20.4/15.9/51.2$, 200 mg, GHSV = 4800 h^{-1}, $T = 400\,^{\circ}C$.

propane into acrylic acid. It should be noted that the addition of tellurium to these catalysts increases yield to acrylic acid.

At intermediate loadings (8 atoms/nm^2), the surface is close to monolayer coverage, which is near 9 atoms/nm^2 in the case of VOx species on an alumina support [56]. Thus, most acid sites from alumina must be titrated. The detected acid sites must originate from supported oxides; their presence clearly decreases upon inert calcinations or upon tellurium addition. Redox sites (formaldehyde) decrease upon inert calcinations for Te-free samples; this is consistent with the much lower binding energies values for molybdenum and vanadium species. The presence of tellurium affects this trend, and the catalyst exhibits much higher redox properties. Inert calcination promotes further entanglement of tellurium ions with molybdenum and niobium ions, leading to the formation of mixed phases. This stabilizes intermediate oxidation states that afford a balance between redox (formaldehyde) and acidic (dimethylether) properties. This appears to favor propane oxidation to acrylic acid.

At high coverages (12 atoms/nm^2), formaldehyde is the main product for all samples, indicative that the major part of active sites on the surface of catalysts are redox, with some acidic sites (DME). At this coverage, crystalline aggregates form, evidenced by XRD (Fig. 1). Inert-calcined Te-free samples are essentially redox (formaldehyde) with few acidic (DME) sites. The presence of tellurium brings a balance between redox and acidic properties. Such balance affords higher yield to acrylic acid; however, activity depends on redox acid balance but also on the catalyst phases. $12Mo_5V_4Nb_1$–air hardly yields any acrylic acid, despite exhibiting similar redox/acid properties balance. This catalyst possesses essentially fully oxidized molybdenum and vanadium species and mixed phases with high-oxidation states. The inert calcination at high coverages forms of MoO_2 and rutile-like phase, visible by XRD and Raman spectroscopy. These phases are able to give redox activity to the catalysts, but such redox sites are not selective to acrylic acid formation (Fig. 4). The surface of air-calcined samples is dominated by Al–Mo–O and Mo–V–O aggregates, identified by XRD (Fig. 1), with low BET surface area values (Table 1). These phases have less redox activity than the dispersed MOx species present in the sample with lower coverage ($8Mo_5V_4Nb_1$–air); thus, the activity during methanol oxidation is lower for the sample with high coverage ($12Mo_5V_4Nb_1$–air). The incorporation of tellurium in the

case of samples with high coverages decreases the activity during methanol oxidation, since the amount of MOx species on the surface decreases. However, the yield to acrylic acid during propane partial oxidation increases. Thus, tellurium is able to interact with molybdenum to form crystalline aggregates visible by XRD (Fig. 1), selective to the acrylic acid formation. At high coverage all the hydroxyl groups from the alumina support must be covered, thus, the acidic activity detected in this case must be due to surface acidic Mo^{6+} and/or Nb^{5+} sites.

5. Conclusions

The combined information on reactive properties (methanol probe) and structural features help understanding structure–activity relationships. These results indicate that methanol probe reaction is a very useful tool to characterize the active centers present on the surface of catalysts, which complement structural characterization data, such as XRD, XPS, UV–vis and Raman spectroscopy.

For the catalysts studied here, combined probe reaction and structural characterization confirm that propane conversion to acrylic acid depends on both structural and reactive features. Efficient catalysts possess both, acid and redox sites and the right kind of structure, such sites are efficient when the catalyst contains mixed oxide phases in which vanadium and molybdenum possess intermediate oxidation states. But when the catalyst contains dispersed oxides or mixed oxides in high-oxidation state, these not work for propane to acrylic acid.

Acknowledgements

COST action D36, WG No. D36/0006/06, the Polish Ministry of Science (Grant No. 118/COS/2007/03) and the Spanish Ministry of Science and Innovation (Grant No. CTQ2008/02461/PPQ) are acknowledged for the financial support. R.L.M. thanks MAEC-AECID (Spain) for his pre-doctoral fellowship and COST D36 for the financial support (STM) during his stay. Authors thank Elizabeth Rojas García (ICP-CSIC) for her help with catalytic tests and to Olaf Torno (SASOL Germany GmbH) for providing alumina support.

References

[1] V.V. Guliants, H.H. Brongersma, A. Knoester, A.M. Gaffney, S. Han, Top. Catal. 38 (2006) 41–50.
[2] M.O. Guerrero-Pérez, T. Kim, M.A. Bañares, I.E. Wachs, J. Phys. Chem. C 112 (2008) 16858–16863.
[3] J.M. Tatibouët, H. Lauron Pernot, J. Mol. Catal. A 171 (2001) 205–216.
[4] L.E. Briand, W.E. Farneth, I.E. Wachs, Catal. Today 96 (2004) 211.
[5] X. Wang, I.E. Wachs, Catal. Today 96 (2004) 211.
[6] I.E. Wachs, J.M. Jehng, W. Ueda, J. Phys. Chem. B 109 (2005) 2275–2284.
[7] S.K. Korhonen, M.A. Bañares, J.L.G. Fierro, A.O.I. Krause, Catal. Today 126 (2007) 235–247.
[8] I.E. Wachs, Y. Chen, J.M. Jehng, L.E. Briand, T. Tanaka, Catal. Today 78 (2003) 13–24.
[9] H. Liu, E. Iglesia, J. Phys. Chem. B 109 (2005) 2155–2163.
[10] J.M. Tatibouët, Appl. Catal. A 148 (1997) 213–252.
[11] S.A.R.K. Deshmukh, M. van Sint Annaland, J.A.M. Kuipers, Appl. Catal. A 289 (2005) 240–255.
[12] M.O. Guerrero Pérez, J.N. Al-Saeedi, V.V. Guliants, M.A. Bañares, Appl. Catal. A 260 (2004) 93–99.
[13] M.O. Guerrero Pérez, L.J. Alemany, Appl. Catal. A 341 (2008) 119–126.
[14] V.V. Guliants, R. Bhandari, J.N. Al-Saeedi, V.K. Vasudevan, R.S. Soman, M.O. Guerrero Pérez, M.A. Bañares, Appl. Catal. A 274 (2004) 123–132.
[15] M.O. Guerrero Pérez, M.C. Herrera, I. Malpartida, M.A. Larrubia, L.J. Alemany, Catal. Today 133–135 (2008) 919–924.
[16] P. Korovchenko, N.R. Shiju, A.K. Dozier, U.M. Graham, M.O. Guerrero-Pérez, V.V. Guliants, Top. Catal. 50 (2008) 43–51.
[17] M.O. Guerrero Pérez, M.A. Bañares, Catal. Today 142 (2009) 245–251.
[18] M.O. Guerrero Pérez, M.A. Bañares, Appl. Catal. A 274 (2004) 123–132.
[19] P. Korovchenko, N.R. Shiju, A.K. Dozier, U.M. Graham, M.O. Guerrero-Pérez, V.V. Gulian, Top. Catal. 50 (2008) 43–51.
[20] B. Kilos, M. Aouine, I. Nowak, M. Ziolek, J.C. Volta, J. Catal. 224 (2004) 314–325.
[21] I. Nowak, M. Ziolek, Chem. Rev. 99 (1999) 3603–3624.
[22] M. Ziolek, Catal. Today 78 (2003) 47–64.
[23] V.V. Atuchin, I.E. Kalabin, V.G. Kesler, N.V. Pervukhina, J. Electron Spectrosc. Relat. Phenom. 142 (2005) 129–134.
[24] M. Ziolek, I. Nowak, Catal. Today 78 (2003) 543–553.
[25] J.F. Moulder, W.F. Stickle, P.E. Sobol, K.D. Bomben, Handbook of X-ray Photoelectron Spectroscopy, Perkin-Elmer, USA, 1992.
[26] R. Häggblad, J.B. Wagner, B. Deniau, J.M.M. Millet, J. Holmberg, R.K. Grasselli, S. Hansen, A. Andersson, Top. Catal. 50 (2008) 52–65.
[27] A.M. Gaffney, S. Chaturvedi, M.B. Clark Jr., S. Han, D. Le, S.A. Rykov, J.G. Chen, J. Catal. 229 (2005) 12–23.
[28] J. Holmberg, S. Hansen, R.K. Grasselli, A. Andersson, Top. Catal. 38 (2006) 17–29.
[29] P. DeSanto Jr., D.J. Buttrey, R.K. Grasselli, W.D. Pyrz, C.G. Lugmair, A.F. Volpe Jr., T. Vogt, B.H. Toby, Top. Catal. 38 (2006) 31–40.
[30] A.M. Venezia, Catal. Today 77 (2003) 359–370.
[31] F. Ivars, B. Solsona, E. Rodríguez Castellón, J.M. López Nieto, J. Catal. 262 (2009) 35–43.
[32] R. Häggblad, J.B. Wagner, S. Hansen, A. Andersson, J. Catal. 258 (2008) 345–355.
[33] G.Ya. Popova, T.V. Andrushkevich, G.I. Aleshina, L.M. Plyasova, M.I. Khramov, Appl. Catal. A 328 (2007) 195–200.
[34] M. Roussel, M. Bouchard, E. Bordes Richard, K. Karim, S. Al-Sayari, Catal. Today 99 (2005) 77–87.
[35] J. Holmberg, R.K. Grasselli, A. Andersson, Top. Catal. 23 (2003) 55–63.
[36] L. Yuan, V.V. Guliants, J. Porous Mater. 16 (2009) 613–622.
[37] N. Haddad, E. Bordes Richard, A. Barama, Catal. Today 142 (2009) 215–219.
[38] M. Roussel, S. Barama, A. Löfberg, S. Al-Sayari, K. Karim, E. Bordes Richard, Catal. Today 141 (2009) 288–293.
[39] N.R. Shiju, V.V. Guliants, Catal. Commun. 9 (2008) 2253–2256.
[40] N.R. Shiju, X. Liang, A.W. Weimer, C. Liang, S. Dai, V.V. Guliants, J. Am. Chem. Soc. 130 (2008) 5850–5851.
[41] P. Botella, A. Dejoz, M.C. Abello, M.I. Vázquez, L. Arrúa, J.M. López Nieto, Catal. Today 142 (2008) 272–277.
[42] M.A. Bañares, I.E. Wachs, J. Raman Spectrosc. 33 (2002) 359–380.
[43] P.A. Spevack, N.S. McIntyre, J. Phys. Chem. 96 (1992) 9029.
[44] G. Mestl, Top. Catal. 38 (2006) 69–82.
[45] G. Mestl, J. Raman Spectrosc. 33 (2002) 333–347.
[46] S.A. Holmes, J. Al-Saeedi, V.V. Guliants, P. Boolchand, D. Georgiev, U. Hackler, E. Sobkow, Catal. Today 67 (2001) 403–409.
[47] L. Yuan, V.V. Guliants, M.A. Bañares, S.J. Khatib, Top. Catal. 49 (2008) 268–280.
[48] X. Yang, W. Zhang, R. Feng, W. Ji, C.T. Au, Catal. Lett. 124 (2008) 288–296.
[49] B. Solsona, M.I. Vázquez, F. Ivars, A. Dejoz, P. Concepción, J.M. López Nieto, J. Catal. 252 (2007) 271–280.
[50] M.O. Guerrero Pérez, M.C. Herrera, I. Malpartida, M.A. Larrubia, L.J. Alemany, M.A. Bañares, Catal. Today 126 (2007) 177–183.
[51] J.M. Oliver, J.M. López Nieto, P. Botella, Catal. Today 96 (2004) 241–249.
[52] P. Botella, E. García González, B. Solsona, E. Rodríguez Castellón, J.M. González Calbet, J.M. López Nieto, J. Catal. 265 (2009) 43–53.
[53] P. Botella, P. Concepción, J.M. López Nieto, Y. Moreno, Catal. Today 99 (2005) 51–57.
[54] B. Solsona, J.M. López Nieto, J.M. Oliver, J.P. Gumbau, Catal. Today 91/92 (2004) 247–250.
[55] P. Botella, A. Dejoz, J.M. López Nieto, P. Concepción, M.I. Vázquez, Appl. Catal. A 298 (2006) 16–23.
[56] I.E. Wachs, L.E. Briand, J.M. Jehng, L. Burcham, X. Gao, Catal. Today 57 (2000) 323–330.